

Article

Exploring the Emergent Redox Chemistry of Pd(II) Nodes with Pendant Ferrocenes: From Precursors, through Building Blocks, to Self-Assemblies

Austin B. Gilbert , Matthew R. Crawley, Trevor J. Higgins , Yuguang C. Li , David F. Watson * 
and Timothy R. Cook * 

Department of Chemistry, University at Buffalo, The State University of New York, Buffalo, NY 14260, USA

* Correspondence: dwatson3@buffalo.edu (D.F.W.); trcook@buffalo.edu (T.R.C.)

Abstract: Energy-relevant small molecule activations and related processes are often multi-electron in nature. Ferrocene is iconic for its well-behaved one-electron chemistry, and it is often used to impart redox activity to self-assembled architectures. When multiple ferrocenes are present as pendant groups in a single structure, they often behave as isolated sites with no separation of their redox events. Herein, we study a suite of molecules culminating in a self-assembled palladium(II) truncated tetrahedron (TT) with six pendant ferrocene moieties using the iron(III/II) couple to inform about the electronic structure and, in some cases, subsequent reactivity. Notably, although known ferrocene-containing metallacycles and cages show simple reversible redox chemistry, this TT undergoes a complex multi-step electrochemical mechanism upon oxidation. The electrochemical behavior was observed by voltammetric and spectroelectrochemical techniques and suggests that the initial Fc-centered oxidation is coupled to a subsequent change in species solubility and deposition of a film onto the working electrode, which is followed by a second separable electrochemical oxidation event. The complicated electrochemical behavior of this self-assembly reveals emergent properties resulting from organizing multiple ferrocene subunits into a discrete structure. We anticipate that such structures may provide the basis for multiple charge separation events to drive important processes related to energy capture, storage, and use, especially as the electronic communication between sites is further tuned.

Keywords: ferrocene; palladium; self-assembly; electrochemistry; supramolecular effects; coupled mechanism; electrochemical oxidation; surface adsorption; electrode passivation



Citation: Gilbert, A.B.; Crawley, M.R.; Higgins, T.J.; Li, Y.C.; Watson, D.F.; Cook, T.R. Exploring the Emergent Redox Chemistry of Pd(II) Nodes with Pendant Ferrocenes: From Precursors, through Building Blocks, to Self-Assemblies. *Inorganics* **2023**, *11*, 122. <https://doi.org/10.3390/inorganics11030122>

Academic Editors: Rainer Winter and Bruno Therrien

Received: 7 February 2023

Revised: 8 March 2023

Accepted: 9 March 2023

Published: 15 March 2023



Copyright: © 2023 by the authors. Licensee MDPI, Basel, Switzerland. This article is an open access article distributed under the terms and conditions of the Creative Commons Attribution (CC BY) license (<https://creativecommons.org/licenses/by/4.0/>).

1. Introduction

The redox and electrochemical properties of ferrocene (Fc) have been well characterized since its discovery in 1951 [1]. The electrochemically reversible and chemically stable ferricenium/ferrocene (Fc⁺/Fc) couple has the potential for applications in charge-transfer mediation, redox switching, sensing, and catalysis [1–4]. For applications that require a specific onset potential, the Fe(III/II) couple can be modified by substitutions on one or both cyclopentadienyl (Cp) rings [5–8]. In addition to altering the electronic structure of the ferrocene, such functionalization may provide the basis for covalent attachment or coordination to surfaces and/or ions. Onset potential notwithstanding, ferrocene and its derivatives are limited to single-electron transfer, which is misaligned with the multi-electron chemistry associated with many small molecule activations such as water splitting, CO₂ reduction, and hydrogen evolution [9–11]. Mediating these transformations demands a fundamental understanding of how to control the multi-redox behavior either using a material that undergoes multi-electron chemistry or by organizing two or more active sites that can operate in concert. The latter has motivated recent efforts to develop multi-ferrocene systems that preserve or enhance the well-defined redox chemistry of this archetypal metallocene [12–17].

Coordination-driven self-assembly is an effective convergent synthetic strategy to organize multiple building blocks into well-defined structures [2]. When one or more tectons are redox-active, self-assembly enables careful control over their proximity and number [18,19]. Common building blocks containing phenyl or ethynyl groups terminating in pyridyl donors are not notably redox-active and so one common method is to covalently tether ferrocene moieties. Alternatively, the metal nodes can house Fc sites, for instance, when 1,1'-bis(diphenylphosphino)ferrocene (dppf) is used as a cis-chelating capping [3]. Free dppf is not stable upon oxidation owing to a dimerization process [20]. When this ligand is coordinated to Pd(II), not only is the redox chemistry preserved, but the oxidative dimerization is also attenuated due to the strong metal—phosphorus bonds that are present [21].

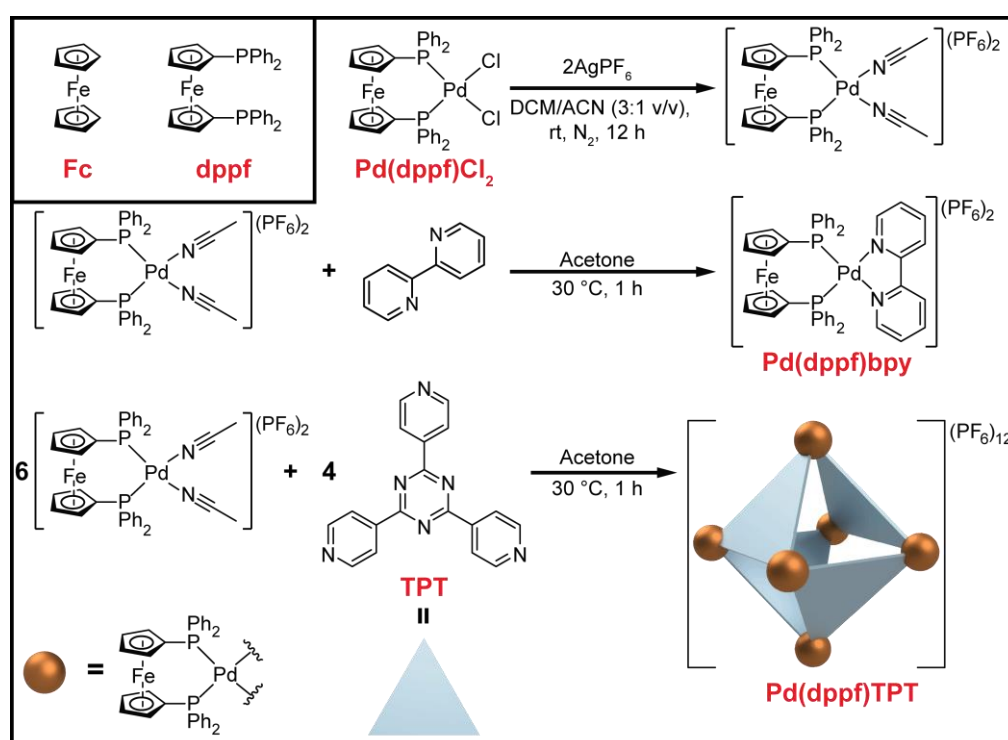
Electrochemical studies of self-assemblies that contain multiple Fc centers commonly conclude that a single, reversible or pseudoreversible oxidation peak is evidence that the ferrocene centers are non-communicative [22–24]. The reversibility is reminiscent of free ferrocene, though the half-cell potentials of these metallacycles and cages are shifted owing to the functionalization of the Cp rings used for tethering. We are interested in exploiting Fc-containing assemblies as multi-electron reservoirs, and our initial studies revealed that the redox response of dppf differs significantly as the coordination environment about a Pd(II) center changes from precursor to building block to assembly. The combination of six dppf-capped Pd(II) building blocks with four 120° tripodal 2,4,6-tri(4-pyridyl)-1,3,5-triazine (TPT) ligands yields a truncated tetrahedron (TT), originally reported by Lees and coworkers and later characterized further by Yang and coworkers [22,25]. Here, we provide evidence of the complex oxidation chemistry of this TT that includes both electrochemical and chemical steps. Voltammetric and spectroelectrochemical techniques suggest that the initial Fc-centered heterogeneous electrochemical oxidation results in a change in species solubility and subsequent deposition of the hexa-Fc TT onto the working electrode. The oxidative response leading to film formation is followed by a second, separable electrochemical oxidation event. The coupled change in solubility and formation of the redox-active film, following initial electrochemical oxidation, is of great significance to further advance analogous materials for catalysis and synthesis applications that require multiple charge equivalents. Furthermore, evaluating the effects of electrochemical redox behavior on solubility and the deposition of redox-active assemblies as thin films is of relevance to film production and the synthesis of electrode materials for heterogeneous catalysis.

2. Results and Discussion

2.1. Synthesis and Spectroscopic Characterization

In order to gain an understanding of how self-assembly may impart emergent redox properties, we constructed a library of precursors, building blocks, and an assembly that spanned Fc, dppf, dichloro (1,1'-bis(diphenylphosphino)ferrocene)palladium(II) ($\text{Pd}(\text{dppf})\text{Cl}_2$), 2,2'-dipyridyl(1,1'-bis(diphenylphosphino)ferrocene)palladium(II) hexafluorophosphate ($\text{Pd}(\text{dppf})\text{bpy}$), and $\text{Pd}(\text{dppf})\text{TPT}$. The final two species were obtained from [bis-acetonitrile(1,1'-bis(diphenylphosphino)ferrocene)palladium(II)] hexafluorophosphate ($[\text{Pd}(\text{dppf})(\text{ACN})_2](\text{PF}_6)_2$) by treatment with the corresponding pyridyl ligand (2,2'-bpy or TPT) in the appropriate stoichiometric ratio (Scheme 1). Immediate color changes of reaction solutions throughout these syntheses indicated that ligand-substitution kinetics were rapid. UV-Vis absorption spectra of the Fc-containing compounds in Scheme 1, on the synthetic pathway to $\text{Pd}(\text{dppf})\text{TPT}$, are presented in Figure S1 in Supporting Information. Treating $\text{Pd}(\text{dppf})\text{Cl}_2$ with silver(I) hexafluorophosphate (AgPF_6) in the presence of acetonitrile (ACN) yielded a pure Pd(II) building block, which was deep blue in color, in stark contrast to the initial reddish-orange solution. The labile ACN could then be readily displaced by pyridyl-based donor ligands to yield mono- and polynuclear complexes in high yields. $[\text{Pd}(\text{dppf})(\text{ACN})_2](\text{PF}_6)_2$ quickly changed from a deep indigo-blue solid to a dark blackish-green solution when solubilized in acetone, likely from the exchange of solvent ligands. The addition of this solution to a clear and colorless solution of 2,2'-bpy

in a 1:1 ratio resulted in a pale purplish-grey solution, evidence for the formation of the Pd(dppf)bpy monomer. These changes in color and intensity of coloration arose from shifts of the visible-wavelength d-d transition of ferrocene and changes in its molar absorption coefficient (ϵ) (Figure S1 in Supporting Information) [26]. The absorption maximum of the d-d band at 440 nm for Fc is at 441 nm for dppf, and red shifts to 464 nm for Pd(dppf)Cl₂ to 573 nm for Pd(dppf)bpy. The measured molar absorption coefficient of this band for dppf ($244 \text{ M}^{-1} \text{ cm}^{-1}$) is similar to our measured value for ferrocene ($103 \text{ M}^{-1} \text{ cm}^{-1}$), whereas the d-d band intensified upon coordination of dppf to Pd(II), with molar absorption coefficients of 705 and $677 \text{ M}^{-1} \text{ cm}^{-1}$ for Pd(dppf)Cl₂ and Pd(dppf)bpy, respectively. The environment of the Pd(II) metal center thus influences the energy and absorptivity of the d-d band. Pd(dppf)bpy also exhibits more strongly-absorbing bands to the blue, including a weak shoulder just red of 350 nm and, in spectra of lower-concentration solutions, absorption bands at 231 nm ($\epsilon = 53,774 \text{ M}^{-1} \text{ cm}^{-1}$) and 304 nm ($\epsilon = 17,163 \text{ M}^{-1} \text{ cm}^{-1}$).



Scheme 1. Fc-containing compounds and synthesis of Pd(dppf)bpy and Pd(dppf)TPT.

When an acetone solution of $[\text{Pd}(\text{dppf})(\text{ACN})_2](\text{PF}_6)_2$ was reacted with TPT in a 3:2 ratio, the reaction mixture changed from dark blackish-green to a much more vibrant light-purple color, an initial indication of the formation of Pd(dppf)TPT. The absorption spectrum of Pd(dppf)TPT (Figure S1e in Supporting Information) is similar to that of Pd(dppf)bpy, with the Fc-centered d-d absorption band centered at 527 nm ($\epsilon = 5960 \text{ M}^{-1} \text{ cm}^{-1}$), red-shifted from that of ferrocene to a lesser extent than for Pd(dppf)bpy. The spectrum of Pd(dppf)TPT also contains a shoulder around 350 nm. The 8.8-fold increase in the molar absorptivity of the Fc-centered band of Pd(dppf)TPT relative to that of Pd(dppf)bpy indicates a degree of electronic communication throughout the assembly, as the absorptivity surpasses that of six individual subunits with pyridyl ligands.

Fc-containing compounds for electrochemical analysis were fully characterized by $^{31}\text{P}\{^1\text{H}\}$ - and ^1H -NMR experiments. $^{31}\text{P}\{^1\text{H}\}$ -NMR spectra are presented in Figure 1, and ^1H -NMR spectra are presented in Figures S2–S4 in Supporting Information. The $^{31}\text{P}\{^1\text{H}\}$ -NMR spectrum of each complex exhibits a sharp singlet with a distinct chemical shift from that of their respective precursor molecules. The sharp singlet observed at 43.03 ppm in the $^{31}\text{P}\{^1\text{H}\}$ -NMR spectrum of $[\text{Pd}(\text{dppf})(\text{ACN})_2](\text{PF}_6)_2$, distinctly shifted downfield from that

of Pd(dppf)Cl₂, suggests the complete displacement of inner-sphere chlorides and equivalently saturated cis-coordination sites. The ³¹P{¹H}-NMR spectrum also contains a septuplet signal far upfield at −142.42 ppm, consistent with the presence of outer-sphere hexafluorophosphate (PF₆[−]) counterions. A sharp shoulder at 1.94 ppm in the ¹H-NMR spectrum (Figure S3 in Supporting Information), downfield from the peak from ACN at 1.94 ppm, is evidence of a coordinated solvent and supports the formation of the cis-ACN product. [Pd(dppf)(ACN)₂](PF₆)₂ was stable to handle in the air when used for synthesis; however, ³¹P{¹H}-NMR signals near 46.0 ppm, assigned to uncharacterized products, developed over the course of days to weeks when stored open to atmosphere. It is possible that the signals arise due to solvent exchange with ambient water to form an aqua species [27–30]. This suggests that the complex should be stored in a dry environment; our precursor was stored in a glovebox when not in use. Clear shifts of the sharp singlets observed in the ³¹P{¹H}-NMR spectra for Pd(dppf)bpy and Pd(dppf)TPT support complete conversion from the cis-ACN acceptor. In ¹H-NMR spectra, there were no resonances associated with residual-free ligands, and the relative integrations of the peaks for the bound ligands were consistent with the proposed structures (Figure S4 in Supporting Information).

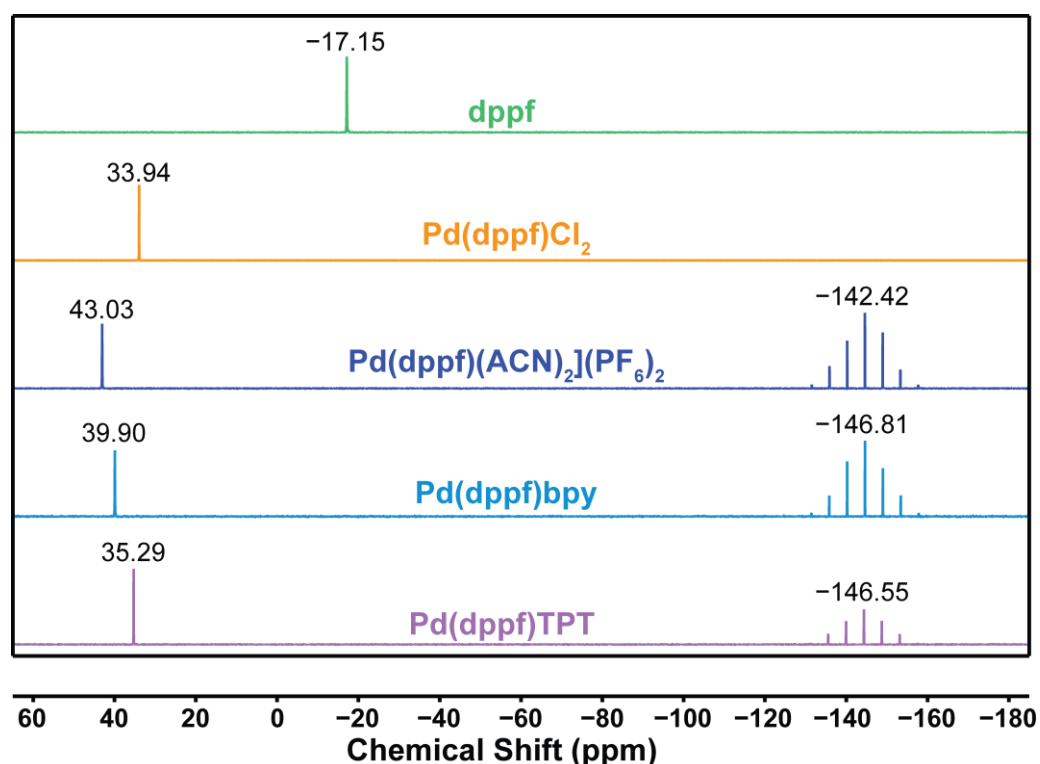


Figure 1. ³¹P{¹H}-NMR spectra of Fc-containing compounds in D₂-DCM. Each spectrum has been normalized to its respective singlet peak.

The DOSY-NMR spectrum of Pd(dppf)TPT in D₂-DCM (Figure S5 in Supporting Information) exhibits a uniform diffusion coefficient for the proton resonances assigned to the metallacage (4.7 and 7.7–8.4 ppm). The diffusion coefficient was estimated to be $\sim 3.53 \times 10^{-10} \text{ m}^2 \text{ s}^{-1}$, which is much lower than the diffusion coefficients estimated from resonances associated with the residual solvents. The diffusion coefficient extracted from our DOSY experiment is lower than the previously reported value of $5.62 \times 10^{-9} \text{ m}^2 \text{ s}^{-1}$ [22]. The difference in diffusion coefficients was attributed to the higher dynamic viscosity of DCM (0.413 mPa s) relative to acetone (0.306 mPa s) [31]. The diameter of the spherical particle approximated by ¹H resonances associated with freely diffusing Pd(dppf)TPT was calculated to be 3.0 nm based on the Stokes—Einstein equation, which is close to the previously approximated value of 3.3 nm [22,32].

2.2. FT-ICR MS

High-resolution FT-ICR MS data for Pd(dppf)bpy display two primary peaks in the full spectrum at m/z values of 961 and 409, attributed to the 1+ and 2+ ions, respectively, of the intact monomer after the loss of PF_6^- counterions (Figure S6 in Supporting Information). The isotopic distribution and m/z values agree with those predicted from simulated data (Figure 2a,b). FT-ICR MS data for Pd(dppf)TPT increased fragmentation relative to Pd(dppf)bpy, its monomeric analog; however, a signal at an m/z of 2173 provides evidence for an intact molecular ion (Figure S7 in Supporting Information), which supports our stoichiometry of self-assembly wherein six Pd(II) and four TPT subunits combine. We can rule out a half-fragment giving rise to this peak because both the isotopic distribution and m/z values match the simulated data (Figure 2c). Taken together, the FT-ICR MS data and the uniform diffusion coefficient obtained from DOSY-NMR strongly support the clean assembly of the desired Pd(dppf)TPT complex.

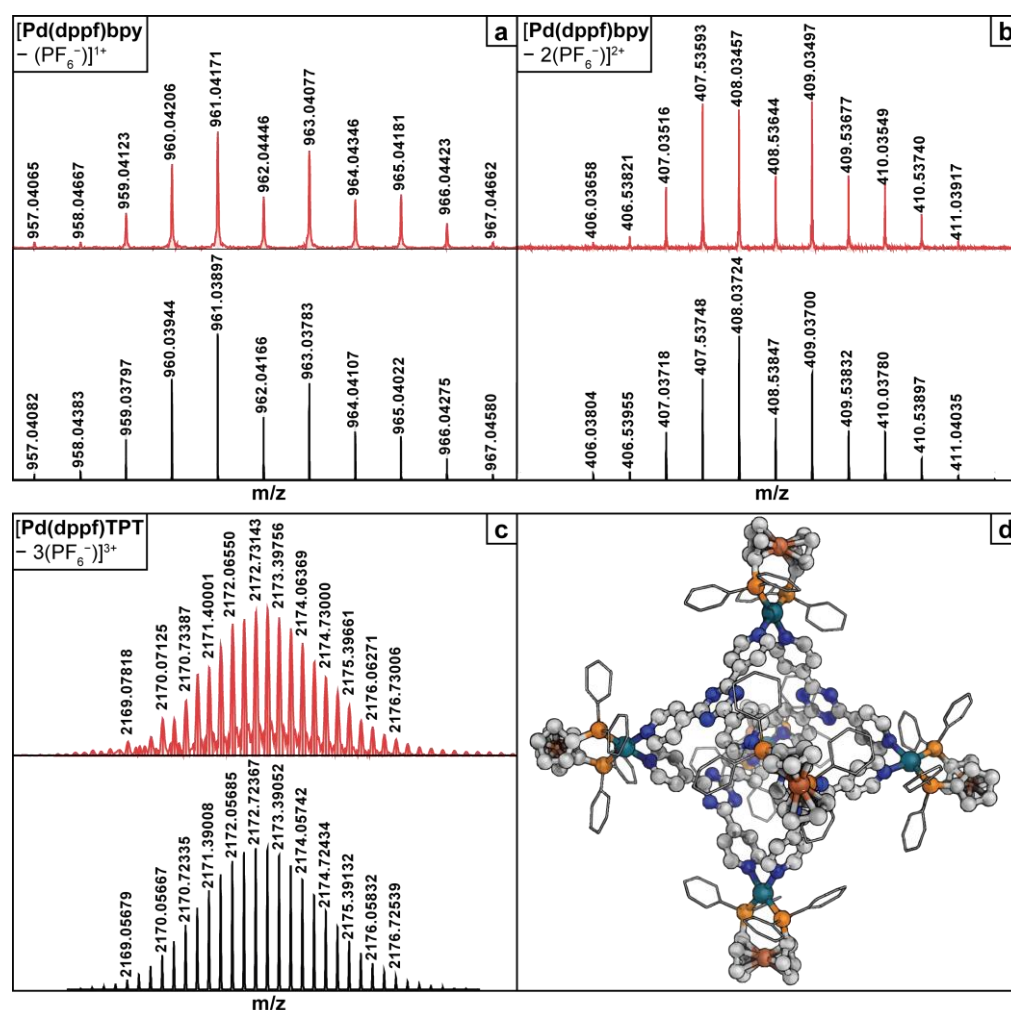


Figure 2. (a–c): Experimental (top, red) FT-ICR and simulated (bottom, black) mass spectra of: (a). $[\text{Pd}(\text{dppf})\text{bpy} - (\text{PF}_6^-)]^{1+}$, (b). $[\text{Pd}(\text{dppf})\text{bpy} - 2(\text{PF}_6^-)]^{2+}$, (c). $[\text{Pd}(\text{dppf})\text{TPT} - 3(\text{PF}_6^-)]^{3+}$. (d). Single crystal structure of Pd(dppf)TPT. Hydrogen atoms are omitted for clarity.

2.3. X-ray Crystal Structure

The structure of Pd(dppf)TPT was determined by single-crystal X-ray diffraction (Figure 2d). The violet crystals were small and poorly diffracting ($d_{\text{min}} = 0.98 \text{ \AA}$). The expected truncated tetrahedron topology was confirmed, with six square planar Pd(II) centers ligated by two pyridyl N-donors and chelated by bis-phosphines on dppf that cap the remaining coordination sites to prevent a divergent geometry. The four TPT ligands

reside in the faces of the truncated tetrahedron. This structure is analogous to other cages that contain six metal nodes and four tritopic donors [33–35].

2.4. Electrochemical Characterization

We used cyclic voltammetry to measure the redox reactivity of the series of complexes shown in Scheme 1. The electrochemical behavior of these complexes was influenced by the Pd(II) coordination environment and further influenced by the polynuclear nature of the TT prism (Figure 3).

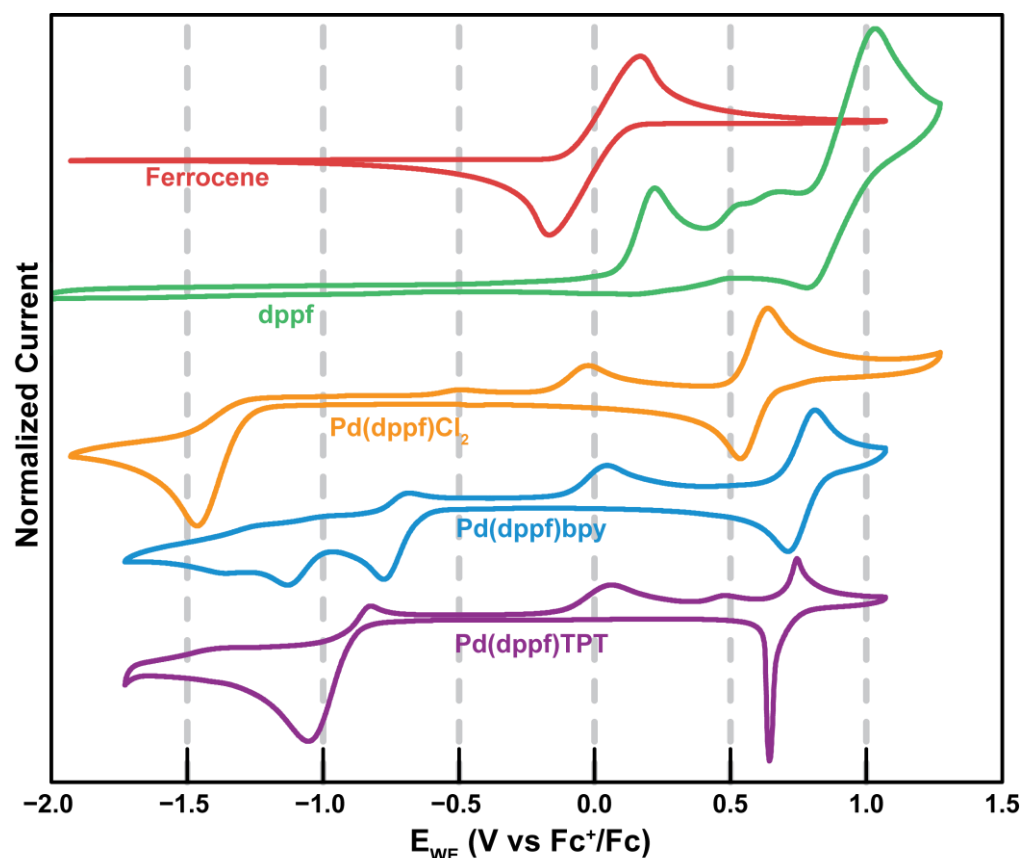


Figure 3. Cyclic voltammograms of Fc-containing compounds (5.0 mM Fc, 1.0 mM dppf, 1.0 mM Pd(dppf)Cl₂, 1.0 mM Pd(dppf)bpy, 0.30 mM Pd(dppf)TPT at 100 mV·s⁻¹ in DCM (100 mM TBAPF₆). Each voltammogram is taken from the second CV cycle, and the current shown for each voltammogram is normalized to the intensity of its respective Fc-centered (first) oxidation peak.

2.4.1. Fc

Under our working conditions, the Fc⁺/Fc couple of free Fc exhibits a peak-to-peak separation of roughly 330 mV, centered at $E_{1/2} = 226$ mV vs. silver/silver(I) nitrate (Ag⁺/AgNO₃). This redox couple was used to standardize all measurements relative to Fc⁺/Fc. The measured peak-to-peak separation is greater than the canonical value of 57 mV for reversible systems, but the ratio of reductive to oxidative charge-passed approaches 1, indicating the electrochemical quasi-reversibility of the system under the reported conditions.

2.4.2. dppf

In comparison, dppf no longer exhibits the same quasi-reversible behavior of the Fc⁺/Fc oxidation as measured for Fc. The peak maximum for the Fe^{III}/Fe^{II} event shifted positively to +219 mV vs. Fc⁺/Fc. At even higher positive potentials, the CV contains a series of irreversible oxidation waves. It has been previously reported that, upon oxidation

of the ferrocene of dppf, the resulting ferricenium center intramolecularly oxidizes a lone pair from one of the pendant phosphines [20]. This radical phosphine then undergoes an intermolecular dimerization with another equivalent of dppf. Thus, it is likely the subsequent irreversible oxidation events are the result of further oxidizing the electrochemical products of the Fc-centered oxidation or subsequently oxidizing the dimerized product. No reduction events were observed within the probed electrochemical window.

2.4.3. Pd(dppf)Cl₂

The reversibility of the Fc⁺/Fc couple was restored upon chelation to the Pd(II) metal center. This result reveals that the lone pairs of free dppf become inaccessible to electrochemical oxidation once bound to Pd(II), with π -backbonding further hindering intramolecular oxidation of the phosphines [20]. The Fc⁺/Fc event of Pd(dppf)Cl₂ was found to shift to +587 mV vs. Fc⁺/Fc. The ratio of the anodic to cathodic current did not vary significantly when the scan rate was decreased from 100 to 10 mV·s⁻¹ (Figures S8 and S9).

2.4.4. Pd(dppf)bpy

The CV of Pd(dppf)bpy is similar to that of Pd(dppf)Cl₂ with some exceptions. The Fc-centered oxidation was shifted even more positively to +763 mV vs. Fc⁺/Fc and remained pseudoreversible as the scan rate was decreased (Figure S10 in Supporting Information). Additionally, the CV contains a bpy-centered reduction event $E_{1/2}$ of -727 mV vs. Fc⁺/Fc (Figure S11 in Supporting Information). The peak-to-peak separation of 90 mV suggested quasi-reversibility. The bpy-centered event is most reversible when it is isolated. At more negative potentials, CVs exhibit an irreversible event, which is associated with a Pd(II)-centered reduction. Since this second reduction is irreversible, it has a deleterious effect on the reversibility of the bpy wave and diminishes the current response of the bpy-centered wave following the first scan (Figure S12 in Supporting Information). Both the cathodic and anodic current responses decrease, likely due to a depletion of Pd(dppf)bpy upon the second reduction.

2.4.5. Pd(dppf)TPT

The arrangement of multiple ferrocene moieties in the TT structure of Pd(dppf)TPT gives rise to quasireversible electrochemical behavior that differs greatly from that of its monomeric analogs (Figure 3). Centered at approximately 713 mV vs. Fc⁺/Fc, the Fe^{III}/Fe^{II} couple of the cage exhibits a peak-to-peak separation of 172 mV at a scan rate of 250 mV·s⁻¹ (Figure 4a). Although oxidation occurs at a similar potential to that of the monomeric derivatives, the wave is asymmetric with respect to both peak shape and current response and exhibits a much larger peak-to-peak separation, which is because electron-transfer kinetics are slow relative to the timescale of the experiment [36]. Following the initial oxidation of Fe(II) to Fe(III), the return reduction wave is sharper and exhibits a higher peak current than the forward oxidation wave. The increased re-reduction current and sharpening of the reduction wave are consistent with the adsorption of the oxidized species onto the electrode surface following electrochemical oxidation [37–39].

To explore these effects further, we acquired CVs of Pd(dppf)TPT, through the Fe(II)-to-Fe(III) oxidation and the return reduction, at varying scan rates (Figure 4b). Full cyclic voltammograms of Pd(dppf)TPT and individual cyclic voltammograms of the Fc-centered oxidation at each scan rate can be found in Figures S13–S20 in the Supporting Information. As the scan rate of the CV measurement decreases from 100 to 10 mV·s⁻¹, the Fc-centered oxidation wave sharpens, and a second oxidation wave develops with a peak shifted ~100 mV more positive than the initial oxidation wave. At intermediate scan rates of 20 and 40 mV·s⁻¹, the second oxidation wave is still measurable as a distinct wave but occurs at more positive potentials than in the 10 mV·s⁻¹ scan. We ascribe the double oxidation not to two kinetically fast events, because they do not coalesce at high scan rates, but rather to the emergence of a subsequent electrochemical oxidation after an intermediate chemical change. This chemical change probably involves adsorption, as evidenced by the peak

shape and asymmetry of the high scan rate data and the sharpening of the cathodic peak with decreasing scan rate, presumably due to a decrease in solubility of the product of the initial Fe(II)-to-Fe(III) electrochemical oxidation [37–39]. The shift of the second oxidation wave to more positive potentials with increasing scan rate implies that the intermediate chemistry occurs slowly relative to electrochemical oxidation.

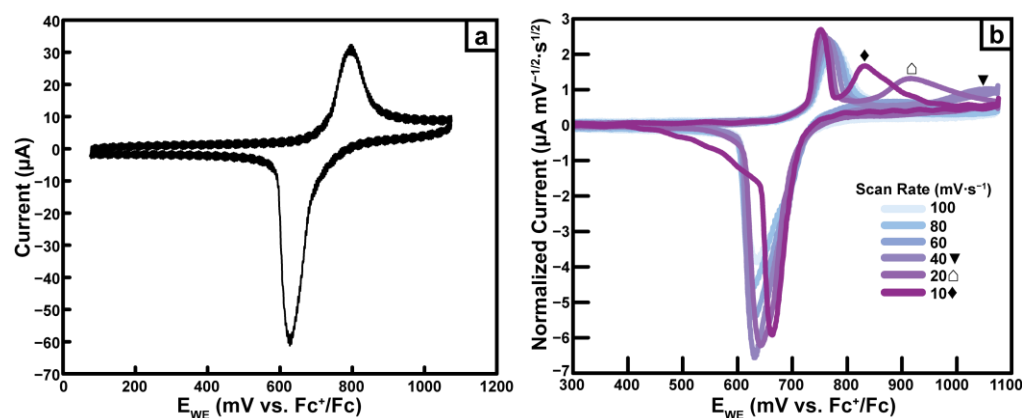


Figure 4. Cyclic voltammograms of Pd(dppf)TPT (0.30 mM) in DCM (100 mM TBAPF₆) acquired within a fixed potential window; shown are the second cycles of each respective scan rate acquisition: (a). CV at a scan rate = 250 mV·s⁻¹. (b). CVs at varying scan rates (10–100 mV·s⁻¹); current is normalized to the scan rate (ν) by dividing by $\nu^{1/2}$.

As the scan rate was changed, the behavior of the reduction peak also changed greatly. The return reduction wave becomes even sharper and shifts to more positive potentials with a decrease in overall peak-to-peak separation. At a scan rate of 100 mV·s⁻¹ for the 0.3 mM Pd(dppf)TPT solution, the reduction wave is broad with a slight shoulder towards positive potentials. The broad, shouldered peak shape suggests a distribution of products being reduced at the electrode near the same potential. As the scan rate was decreased at this concentration, the overall peak shape became much sharper and more well-defined, with the reduction peak in the 10 mV·s⁻¹ scan shifting to more positive potentials by nearly 30 mV. This better-defined reduction peak is centered on the shoulder seen in CVs acquired at 100 mV·s⁻¹, with a broad tail towards more negative potentials, spanning a potential window of roughly 250 mV.

The relationship between peak current and the square root of the scan rate was linear for the first anodic wave (Figure S21 in Supporting Information). This linear relationship suggests that the first oxidation event is diffusion-limited, according to the Randles—Sevcik equation [36]. Therefore, Pd(dppf)TPT undergoes the first electrochemical oxidation as a freely-diffusing species in solution, and this event precedes any adsorption phenomenon. The peak current for the cathodic wave did not exhibit the same linear relationship with the square root of the scan rate, suggesting that the reduction event is a non-diffusion-limited event (Figure S21 in Supporting Information).

The correlation between the first oxidation and the apparent film-formation step was further probed by changing the switching potentials of CVs, such that the first oxidation was fully observed at each scan rate, but the direction of the potential sweep was reversed before the onset of the subsequent oxidation (Figure 5a). As such, the chemical step induced by the initial oxidation could still proceed, but the applied potential was swept reductively before further oxidation could occur. CVs acquired at high scan rates are consistent with a quasi-reversible Fc-centered oxidation. In these data, the broad reduction wave is attributed primarily to the reduction of ferricenium generated from the first electrochemical oxidation. The broad peak shape suggests a distribution of products; thus, the mechanistic steps following the initial oxidation may occur to some extent, even at high scan rates. Notably, CVs acquired at the slowest scan rates of 5–10 mV·s⁻¹ contained positively shifted, sharp, and intense reduction peaks, revealing that the sharpening and enhancement of the return

reduction peak, which are indicative of the adsorption of oxidation products to the electrode, resulting from the first electrochemical oxidation and, thus, that the oxidation events at higher potentials are likely attributable to adsorbed species.

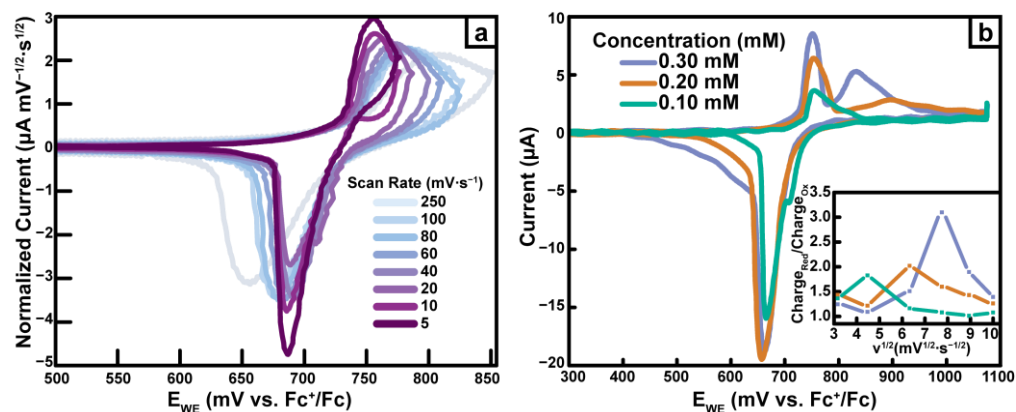


Figure 5. (a). Cyclic voltammograms of Pd(dppf)TPT (0.30 mM) with varying potential window and scan rate (5–250 mV·s⁻¹) in DCM (100 mM TBAPF₆); current is normalized to the scan rate (ν) by dividing by $\nu^{1/2}$. (b). Cyclic voltammograms of Pd(dppf)TPT (0.10–0.30 mM) at 10 mV·s⁻¹ in DCM (100 mM TBAPF₆); the inset shows a plot of Charge_{Red}/Charge_{Ox} vs. $\nu^{1/2}$. Each voltammogram is taken from the second CV cycle.

To further elucidate the nature of the oxidation-induced chemical step, we investigated the concentration-dependence of the coupled oxidation events. Interestingly, concentration-dependent CVs (Figure 5b) exhibit similar features as the aforementioned scan-rate-dependent CVs (Figure 6). CVs acquired at lower concentrations resemble those acquired at fast scan rates. In other words, the second oxidation exhibits a decreased current response and a more positive potential either when the scan rate is high or when the concentration is low.

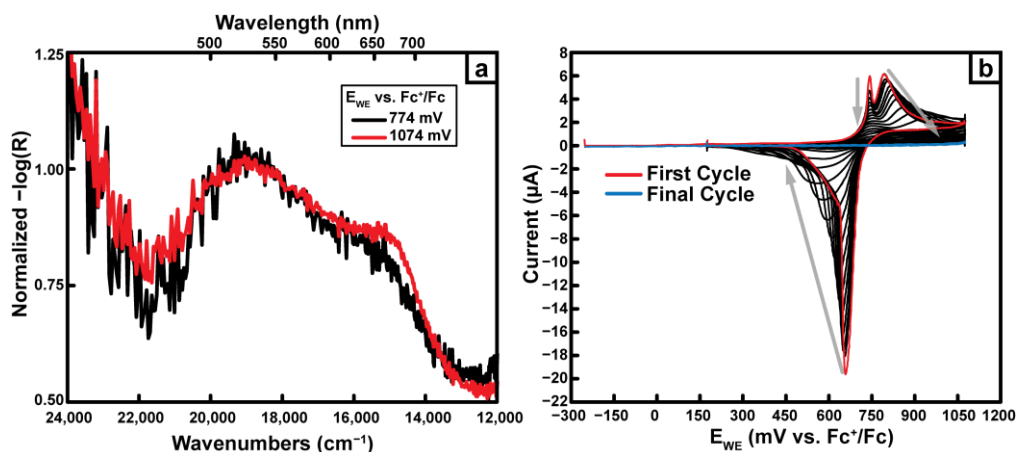


Figure 6. (a). Diffuse reflectance spectra of FTO working electrodes modified with adsorbed Pd(dppf)TPT following electrolysis at the indicated potential. Spectra are normalized to the 527 nm absorbance band of the native Pd(dppf)TPT species. (b). Cyclic voltammograms (50 total cycles) of 0.30 mM Pd(dppf)TPT in DCM (100 mM TBAPF₆) at a scan rate of 10 mV·s⁻¹. Alternating cycles have been omitted for clarity.

The ratio of the total cathodic charge passed to the total anodic charge passed (Charge_{red}:Charge_{ox}) varied with both scan rate and concentration of the system (Figure 5b inset). For Pd(dppf)TPT at a concentration of 0.30 mM, Charge_{red}:Charge_{ox} was 1.4 at 100 mV·s⁻¹, increased to a maximum of 3.1 at 60 mV·s⁻¹, and then decreased to 1.2 at 10 mV·s⁻¹. Although the ratio approached 1.0 at slower scan rates, the reductive charge passed exceeded

the oxidative charge passed at all scan rates. The scan rate with the maximum value of $\text{Charge}_{\text{red}}:\text{Charge}_{\text{ox}}$ varied with concentration. Maximum $\text{Charge}_{\text{red}}:\text{Charge}_{\text{ox}}$ ratios were 3.1 at $60 \text{ mV}\cdot\text{s}^{-1}$ for the 0.30 mM system, 2.0 at $40 \text{ mV}\cdot\text{s}^{-1}$ for 0.20 mM system, and 1.8 at $20 \text{ mV}\cdot\text{s}^{-1}$ for the 0.10 mM system. When the second oxidation event is limited, at high scan rates, low concentrations, or both, $\text{Charge}_{\text{red}}:\text{Charge}_{\text{ox}}$ is much greater than 1.0. The observed trends are thus further consistent with adsorption of the initially oxidized products to the electrode surface, where the $\text{Charge}_{\text{red}}:\text{Charge}_{\text{ox}}$ ratio increases with scan rate [40].

CV data for Pd(dppf)TPT consistently exhibit a sharpening of both the initial Fc-centered oxidation and the return reduction wave with increasing concentration or decreasing scan rate. The sharpening of waves, narrowing peak-to-peak separations, and non-unity values of $\text{Charge}_{\text{red}}:\text{Charge}_{\text{ox}}$ are consistent with a non-diffusion limited process [37–40]. In the case of this system, these data suggest that the initially oxidized species is less soluble than Pd(dppf)TPT, which leads to the adsorption of the product of the initial oxidation to the electrode surface.

2.5. UV-Vis Spectroelectrochemistry

In an attempt to characterize the products of oxidation and potential subsequent steps, we performed UV-Vis spectroelectrochemical measurements, in which absorption spectra of electrolyte solutions were acquired as a function of applied potential during the acquisition of cyclic voltammograms. For both Fc and Pd(dppf)Cl₂, following electrochemical oxidation, a new absorption band developed at lower energies relative to the d-d band of the unoxidized species (Figure S22a,b in Supporting Information). This new band, which was centered at 620 and 616 nm for Fc and Pd(dppf)Cl₂, respectively, is attributed to the LMCT transition of ferricenium moieties produced by electrochemical oxidation [26,41]. In contrast, the spectra for oxidized Pd(dppf)TPT do not contain an analogous ferricenium-derived LMCT band (Figure S22d,c in the Supporting Information). For Pd(dppf)TPT, over the course of the CV experiment, the only notable change in the absorption spectrum was the development of more pronounced bands at wavelengths less than 450 nm. Thus, on the timescale of this experiment, there was no spectroscopic evidence for the formation of soluble Pd(dppf)TPT cages containing oxidized ferricenium moieties. UV-Vis spectra of electrolyte solutions with relatively higher concentrations of Pd(dppf)TPT (0.30 mM), acquired under oxidizing conditions, exhibited an elevated baseline (Figure S22d in the Supporting Information), consistent with increased scattering of light caused by precipitation of oxidation products. Oxidation-induced precipitation is consistent (a) with the absence of a measurable LMCT band of solvated Fc⁺-containing species and (b) with a mechanism in which electrochemically-oxidized Pd(dppf)TPT with pendant ferricenium is insoluble in the electrolyte and adsorbs to the working electrode's surface.

2.6. Diffuse Reflectance Spectroelectrochemistry

We next endeavored intentionally to prepare thin films of oxidized Pd(dppf)TPT on FTO via constant-potential deposition from an electrolyte solution containing Pd(dppf)TPT. To characterize the extent of oxidative adsorption of Pd(dppf)TPT, we acquired diffuse reflectance UV-Vis spectra of FTO working electrodes after prolonged oxidation (Figure 6a). Prolonged oxidation indeed produced a film on FTO, which was apparent by eye and grey in color (Figure S23 in the Supporting Information). Reflectance spectra of film-coated working electrodes exhibited a broad absorption from approximately 450 to 700 nm, consistent with the d-d transition of Fc centered at 527 nm for Pd(dppf)TPT, as well as a lower-energy band centered at approximately 650 nm, which we attribute to the LMCT transition of Fc⁺-containing oxidation products of Pd(dppf)TPT. The presence of spectral features associated with Pd(dppf)TPT and Fc⁺, in spectra of the films on FTO, provides additional evidence for a mechanism in which the initial products of oxidation of Pd(dppf)TPT are deposited onto the working electrode surface. Prolonged reduction in the

modified FTO working electrode resulted in a clean FTO film that was completely removed of any deposited Pd(dppf)TPT by eye (Figure S23 in the Supporting Information).

2.7. CV Cycling

Repeated CV cycling of Pd(dppf)TPT reveals a depletion of current across the first Fc-centered oxidation, the second oxidation, and the return reduction, as well as associated shifts of the second oxidation wave positively and the return reduction event negatively (Figure 6b). Within the context of our proposed mechanism, as oxidation–reduction cycles are repeatedly swept, the first oxidation event should result in ongoing adsorption of the oxidized product to the working electrode surface. The current response of the initial oxidation will thus be depleted with repeat cycles as adsorption sites on the working electrode surface become occupied by the Fc⁺-containing species. Over the course of the CV cycling experiment, the second oxidation wave shifts to more positive potentials, as expected if the second wave corresponds to the further oxidation of partially oxidized, adsorbed Pd(dppf)TPT. Similarly, the return reduction wave shifts to more negative potentials, and the current response of both waves steadily decreases. The increasing peak-to-peak separation may also indicate that electron-transfer kinetics are slower at the modified glassy carbon surface, perhaps arising from decreased coupling between the electrode and remaining Fc sites on partially oxidized, adsorbed species [42]. By the end of the repetitive cycling experiment, the current response from both oxidation and reduction events was completely depleted until no charge was passed.

2.8. Proposed Mechanism

One overall mechanism that is consistent with all our data is as follows. The initial electrochemical oxidation wave corresponds to the oxidation of one or more ferrocene centers of Pd(dppf)TPT, yielding a species which, due to its decreased solubility in the electrolyte solution, then adsorbs to the working electrode (either glassy carbon or FTO as evidenced by both CV and diffuse reflectance measurements). Importantly, though, the initial oxidation wave in CVs is not separable, even at high scan rates, which would be expected if ferrocene groups of Pd(dppf)TPT were coupled. Adsorption of oxidized Pd(dppf)TPT alters the surface of the electrode, whether it is glassy carbon or FTO. This change in surface chemistry is likely the cause of the second oxidation event in measured cyclic voltammograms. This second oxidation event may involve either: (1) the oxidation of remaining Fc moieties on the partially-oxidized Fc⁺-containing Pd(dppf)TPT adsorbate, or (2) the heterogeneous oxidation of remaining Pd(dppf)TPT in solution at the surface-modified working electrode. Results from the cycling experiment with glassy carbon (Figure 6b) suggest that the working electrode surface becomes incapable of interacting heterogeneously with the analyte solution once it has been fully passivated by adsorbed products, ruling out the likelihood of mechanism (2) for the second oxidation. Although Fc⁺ is present initially, the passivation of the electrode with a redox-silent adsorbent is consistent with the oxidized cage decomposing to its building blocks. Since TPT is neither soluble nor redox-active under these conditions and potential windows, it is the most likely candidate for the loss of the current response. Related C₃ symmetric tripyridyl molecules have shown an affinity for carbon surfaces, stabilized by intermolecular H-bonding and substrate-adsorbate interactions that result in dense ordering that fully covers the carbon surface [43].

3. Materials and Methods

3.1. Materials

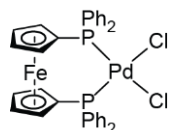
The chemicals ferrocene (Fc) [Sigma Aldrich], dichloro(1,5-cyclooctadiene)palladium(II) (Pd(COD)Cl₂) [Strem], 1,1'-bis(diphenylphosphino)ferrocene (dppf) [Matrix Scientific], silver(I) hexafluorophosphate (AgPF₆) [Oakwood Chemical], silver(I) nitrate (AgNO₃) [Fisher Scientific], 2,2'-bipyridine (2,2'-bpy) [Chem Impex Int'l Inc.], 2,4,6-tri(4-pyridyl)-1,3,5-triazine (TPT) [TCI], and tetra(n-butyl)ammonium hexafluorophosphate (TBAPF₆)

[Oakwood Chemical] were used as-received and without further purification. Glass sheets with a thickness of 2.25 mm and coated with fluorine-doped tin oxide (FTO) were sourced from Pilkington. Dichloromethane (DCM) was sourced from JT Baker, whereas the acetonitrile (ACN), acetone, diethyl ether (Et₂O), and hexanes were all sourced from Fisher Chemical. Solvents were used as received and without purification unless the use of a dry solvent was specified. Dry solvents were dispensed from a Glass Contour Solvent System assembled by Pure Process Technologies LLC (Nashua, NH, USA).

3.2. NMR Experiments

All ¹H-NMR experiments were conducted on a Bruker Avance Neo 400 MHz instrument operated at 400 MHz, and all chemical shifts (δ) are reported in parts per million (ppm) in reference to the residual protio-solvent peak. ³¹P{¹H}-NMR experiments were conducted on the same instrument operated at 162 MHz, and all chemical shifts (δ) are reported relative to an 85% H₃PO₄ standard. All NMR solvents were sourced from Cambridge Isotope Laboratories, Inc. (Tewksbury, MA, USA). Dichloromethane-D₂ (CD₂Cl₂) and acetonitrile-D₃ (CD₃CN) ampules were used without further purification, whereas acetone-D₆ (CO(CD₃)₂) was dried over 3 Å molecular sieves.

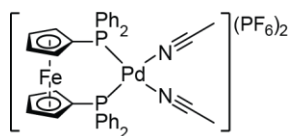
3.3. Synthesis of dichloro(1,1'-bis(diphenylphosphino)ferrocene)palladium(II) (Pd(dppf)Cl₂)



A solution of Pd(COD)Cl₂ (412.3 mg, 144.4 μmol, 1.0 equivalents) in dry DCM (~15 mL) was prepared in a round bottom flask and, using standard Schlenk techniques, was placed under a nitrogen (N₂) atmosphere with five vacuum/N₂ cycles and left to stir. The dppf (800.6 mg, 144.4 μmol, 1.0 equivalents) was dissolved in minimal dry DCM (~2 mL), and added to the stirred solution of Pd(COD)Cl₂, rinsing with 1 mL of dry DCM three additional times to ensure complete transfer. The reaction mixture was then subjected to another five vacuum/N₂ cycles and allowed to stir overnight at rt. The solvent was then removed from the reaction mixture under vacuum (50 °C, 300–400 mbar), and the resulting solid was redissolved in a minimal amount of DCM, and then precipitated with the addition of hexanes (3:1 hexanes:DCM v:v) and centrifuged to collect the solid precipitate. The product was further washed by the addition of hexanes with sonication to redisperse the powder in the wash solvent, and once again centrifuged to collect the solid. This wash procedure was repeated a minimum of three times to ensure the complete removal of residual COD. The product was then dried in vacuo and isolated as an orange-red powder (1038 mg, 98% yield). ¹H-NMR (400 MHz, CD₂Cl₂, 300 K): δ = 7.93 (dd, 8 H, Ph H_o), 7.58 (t, 4 H, Ph H_p), 7.49 (dd, 8 H, Ph H_m), 4.46 (s, 4 H, Fc H_α), 4.27 (s, 4H, Fc H_β) ppm. ³¹P{¹H}-NMR (162 MHz, CD₂Cl₂, 300 K): 33.94 (s, PPh₂) ppm. ε = 705 (λ = 464 nm) M⁻¹·cm⁻¹.

3.4. Synthesis of

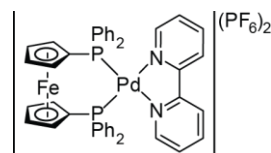
[bis-acetonitrile(1,1'-bis(diphenylphosphino)ferrocene)palladium(II)]hexafluorophosphate [(Pd(dppf)(ACN)₂](PF₆)₂)



In a glove box under an N₂ atmosphere, Pd(dppf)Cl₂ (101.1 mg, 137.8 μmol, 1.0 equivalents) was dissolved in dry DCM (~8 mL) and stirred at rt in a 20 mL scintillation vial. Then, AgPF₆ (69.7 mg, 276 μmol, 2.0 equivalents) was separately dissolved in dry ACN (~2 mL). The AgPF₆ solution was added to the stirred solution of Pd(dppf)Cl₂. The reaction mixture was left to stir overnight in the glovebox at rt. Upon completion, the

reaction mixture was kept under the inert atmosphere of the glovebox while the silver chloride (AgCl) precipitate was removed. AgCl was gravity filtered from the solution using a small microfiber disc carefully packed into a pipette, loosely topped with a 1–2 cm celite plug. The filtrate was then filtered a second time in the same manner and equally distributed into 2 dram vials in 1–2 mL aliquots. The product was then precipitated by the addition of Et₂O in a ~5-fold excess to the filtrate solution, and the deep violet solution became cloudy. The vials were then brought out of the glovebox and quickly sonicated in order to promote complete precipitation, which was evident by a color change from the cloudy violet solution to a much more vibrant deep blue. The precipitate was then collected by centrifugation. The isolated product was washed by the addition of Et₂O, with sonication to redisperse the powder in the wash solvent, and then collected by centrifugation. This wash process was repeated a minimum of three times. The product was then dried in vacuo and isolated as a deep violet-blue powder (113.9 mg, 80% yield). ¹H-NMR (400 MHz, CD₃CN, 300 K): δ = 7.77 (m, 12 H, Ph H_o and H_p), 7.60 (dd, 8 H, Ph H_m), 4.76 (s, 4 H, Fc H_α), 4.58 (s, 4 H, Fc H_β) ppm. ³¹P{¹H}-NMR (162 MHz, CD₃CN, 300 K): δ = 43.03 (s, PPh₂), −142.42 (m, PF₆[−]) ppm.

3.5. Synthesis of 2,2'-dipyridyl(1,1'-bis(diphenylphosphino)ferrocene)palladium(II) hexafluorophosphate (Pd(dppf)bpy)



Open to the air, 2,2'-bpy (2.40 mg, 15.2 μmol, 1.6 equivalents) was dissolved in acetone (5 mL) and stirred at rt in a 20 mL scintillation vial. [Pd(dppf)(ACN)₂](PF₆)₂ (15.7 mg, 15.2 μmol, 1.0 equivalents) was separately dissolved in acetone (~5 mL). The resulting solution, which changed from deep violet-blue to greenish-black, was rapidly pipetted into the stirred solution of 2,2'-bpy. The flask was rinsed with minimal acetone (~1 mL) three additional times to ensure complete transfer. The reaction mixture quickly turned light-purple upon the addition of the Pd precursor. The reaction was stirred at 30 °C for 1 h. The solvent was then removed under vacuum (50 °C, 300–400 mbar), and the solid was redissolved in minimal acetone (1–3 mL), precipitated with an excess of Et₂O (3:1, Et₂O:acetone, v:v), and collected by centrifugation. The product was further washed by the addition of Et₂O to the isolated solid, with sonication to redisperse the powder in the wash solvent, and the solid product was once again collected via centrifugation. This wash process was repeated a minimum of three times. The product was then dried in vacuo and isolated as a greyish-purple solid (14.6 mg, 87% yield). ¹H-NMR (400 MHz, CD₃CN, 300 K): δ = 8.17 (d, 2 H, bpy), 8.04 (dd, 2 H, bpy), 7.92 (dd, 8 H, Ph H_o), 7.81 (s, 2 H, bpy), 7.56 (dd, 4 H, Ph H_p), 7.43 (dd, 8 H, Ph H_m), 7.07 (dd, 2H, bpy), 4.80 (s, 4 H, Fc H_α), 4.69 (s, 4 H, Fc H_β) ppm. ³¹P{¹H}-NMR (162 MHz, CD₃CN, 300 K): δ = 39.90 (s, PPh₂), −146.81 (m, PF₆[−]) ppm. ε = 53,774 (λ = 231 nm), 17,163 (λ = 304 nm), 677 (λ = 573 nm) M^{−1}·cm^{−1}.

3.6. Synthesis of Pd(dppf)TPT

The synthetic procedure was adapted from the literature [22,25]. Modified reaction conditions were used, including elevating temperature and increasing reaction time to ensure complete conversion, as well as a modified work-up using centrifugation for collection and washing of the isolated product. Open to the air, TPT (29.7 mg, 95.7 μmol, 2.0 equivalents) was dispersed in acetone (~5 mL) and stirred at rt in a 20 mL scintillation vial. [Pd(dppf)(ACN)₂](PF₆)₂ (148.2 mg, 143.5 μmol, 3.0 equivalents) was separately dissolved in acetone (~5 mL). The solution, which changed from deep violet-blue to greenish-black, was rapidly pipetted into the stirred solution of TPT. The flask was rinsed with acetone (~1–3 mL) three additional times to ensure complete transfer. The reaction mixture quickly turned light-purple upon the addition of the Pd precursor. The reaction

was left to stir at 30 °C for 1 h. The solvent was then removed under vacuum (50 °C, 300–400 mbar), and the solid was redissolved in acetone (~1–3 mL) and gravity filtered through a small microfiber disc carefully packed into a pipette. The product was then precipitated in an excess of hexanes (3:1, hexanes:acetone, v:v), and the solid was collected by centrifugation. The product was further washed by the addition of hexanes to the isolated solid, sonicated to redisperse the powder in the wash solvent, and once again centrifuged to collect the solid. This wash process was repeated a minimum of three times. The product was then dried *en vacuo* and isolated as a light-purple solid (118.1 mg, 71% yield). ¹H-NMR (400 MHz, CD₂Cl₂, 300 K): δ = 8.37 (d, J = 10 Hz, 24 H, pyridyl H_α), 7.97 (d, J = 10 Hz, 24 H, pyridyl H_β), 7.75 (m, 72 H, Ph H_o and H_p), 7.66 (dd, 48 H, Ph H_m), 4.69 (d, 48 H, Fc H_α and H_β) ppm. ³¹P{¹H}-NMR (162 MHz, CD₂Cl₂, 300 K): 35.29 (s, PPh₂), −146.55 (m, PF₆[−]) ppm. ε = 5963 (λ = 527 nm) M^{−1}·cm^{−1}.

3.7. UV-Vis

UV-Vis spectra were acquired with a Cary 8454 UV-Vis diode array system. A quartz cuvette with a path length of 1 cm was used for all measurements. All samples for absorbance measurements were prepared open to air and using dry DCM.

3.8. Mass Spectrometry

Mass spectra were acquired using electrospray ionization with a home-built sprayer into a Bruker Solarix 12 T Fourier transform-ion cyclotron resonance mass spectrometer (FT-ICR MS) (12 Tesla FT-ICR) system equipped with a dual source.

3.9. Crystallographic Details

The datum crystal of approximately 0.1 mm × 0.1 mm × 0.05 mm was mounted on a Rigaku XtaLAB Synergy diffractometer coupled to a Rigaku HyPix detector with Cu Kα radiation (λ = 1.54184 Å) from a PhotonJet micro-focus X-ray source at 100 K. The diffraction images were processed and scaled using the CrysAlisPro software [44]. Structure solution was obtained in Olex2 using ShelXT via intrinsic phasing [45]. Least squares refinement was performed by ShelXL [46]. The crystals of Pd(dppf)TPT were small and poorly diffracting. Diffraction to the IUCr “publishable limit” was not achievable, as is often the case for supramolecular metallacages. Completeness of the data set was less than 100%; however, this does not detract from the conclusions of this study, namely, that the desired metallacages were formed in the anticipated atomic arrangement.

3.10. Electrochemical Measurements

All electrochemical experiments were carried out using a BioLogic SP-200 or SP-300 potentiostat. Working and counter electrodes were sourced from CH Instruments, and reference electrodes were sourced from BASi. TBAPF₆ was recrystallized three times from absolute ethanol, dried under vacuum, and used as the supporting electrolyte. The three-electrode cell consisted of a 3.0 mm glassy carbon-disc working electrode, a 0.5 mm diameter platinum wire counter electrode, and a non-aqueous Ag/AgNO₃ reference electrode constructed of a 4.0 mm glass tube housing a 0.5 mm Ag wire submerged in a 100 mM TBAPF₆ ACN electrolyte containing 10 mM AgNO₃. All analyte solutions were prepared at the indicated concentrations in a 100 mM TBAPF₆ electrolyte solution of dry DCM. Analyte solutions were placed under an inert N₂ atmosphere, either by sparging or by conducting measurements in a glovebox. Sparged samples were prepared by bubbling N₂ for 10 min prior to any measurements in order to degas the solvent, pre-bubbling through neat solvent to minimize analyte concentration changes. Positive N₂ pressure was maintained in the headspace of the electrochemical cell for the duration of any data acquisition. The glassy carbon electrode was polished between each measurement performed on a given analyte solution while bubbling the analyte solution with N₂ to maintain the air-free environment. Integrations to determine the charge passed in CV experiments were performed in BioLogic

EC-Labs software. Linear regression fits were used to establish the baseline current before either the oxidative or reductive peaks were integrated.

3.11. UV-Vis Spectroelectrochemistry

UV-Vis spectroelectrochemistry experiments were conducted using a Pine Research WaveDriver 40 potentiostat/galvanostat and an Avantes AvaSpec UV-vis spectrophotometer. TBAPF₆ was recrystallized three times from absolute ethanol, dried under vacuum, and used as the supporting electrolyte. Samples for measurement were prepared at 1.8 mM Fc, 1.8 mM Pd(dppf)Cl₂, and 0.04 or 0.30 mM Pd(dppf)TPT in dry DCM (100 mM TBAPF₆). The Pine Honeycomb UV-vis Spectroelectrochemical Cell (part# AB01STC1PT) consists of a built-in platinum honeycomb working electrode and two platinum counter electrode bands. A non-aqueous Ag/AgNO₃ reference electrode was used, constructed of an Ag wire submerged in a 100 mM TBAPF₆ ACN electrolyte containing 10 mM AgNO₃. Samples were purged with N₂ to deoxygenate before measurements. Spectra were recorded in a 1.7 mm quartz cuvette. Parameters for measurements included a 0.03 s integration time, a boxcar width of 10, and an averaging of 50 samples.

3.12. Diffuse Reflectance Spectroelectrochemistry

Diffuse reflectance spectroelectrochemistry experiments were conducted using a Biologic SP-200 potentiostat and an Agilent 8453 UV-Vis diode array equipped with a Labsphere RSA-HP-8453 integrating light sphere. Sample preparation and electrochemical techniques were carried out under an N₂ glovebox atmosphere. Diffuse reflectance spectra of samples after electrochemical techniques were acquired in open atmosphere and blanked on a bare FTO film. The counter electrode was sourced from CH Instruments, and the reference electrode was sourced from BASi. TBAPF₆ was recrystallized three times from absolute ethanol, dried under vacuum, and used as the supporting electrolyte. Blank FTO films were prepared from the coated glass sheets and cut to approximately 40 × 14.5 × 2.5 mm. The analyte solution was 0.30 mM Pd(dppf)TPT in dry DCM with 100 mM TBAPF₆. A three-electrode H-cell was assembled, with the two compartments separated by a glass frit. The working electrode compartment consisted of an FTO-coated glass slide as the working electrode, submerged in the analyte solution while stirred. The opposite compartment consisted of blank 100 mM TBAPF₆ DCM electrolyte, the platinum mesh counter electrode, and the reference electrode. A non-aqueous Ag/AgNO₃ reference electrode was used, consisting of an Ag wire submerged in a 100 mM TBAPF₆ ACN electrolyte containing 10 mM AgNO₃. Chronocoulometry was carried out at the indicated potentials for 30 min. The working electrode was then removed from the H-cell, rinsed with the blank electrolyte solution, and removed from the glovebox to record diffuse reflectance spectra of the electrodeposited film.

4. Conclusions

The synthesis of the novel complex Pd(dppf)bpy was supported by NMR, ESI-FT-ICR MS, and UV-Vis experiments. The Fc-centered absorption band was enhanced by a factor of 6.6 because of the coordination environment of dppf. CVs of Pd(dppf)bpy exhibited a pseudoreversible Fc-centered oxidation with no evidence of any coupled chemical mechanism. CVs acquired at reductive potentials exhibited irreversible Pd^{II}-centered waves, similar to CVs of Pd(dppf)Cl₂, as well as a pseudoreversible bpy-centered reduction.

The previously reported self-assembled complex Pd(dppf)TPT was obtained cleanly, as evidenced by NMR, ESI-FT-ICR MS, and UV-Vis experiments. The Fc-centered absorption band was enhanced by 8.8-fold relative to that of Pd(dppf)bpy, suggesting supramolecular effects as the molar absorptivity of the band surpassed the sum of those of six monomeric analogs. The structure of Pd(dppf)TPT was determined crystallographically to confirm the expected TT topology of the 6 dppf-capped square planar Pd(II) metal centers, with the cis-coordinated TPT ligands occupying the alternating faces of the prism. CV measurements revealed evidence for a pseudoreversible Fc-centered oxidation, which is coupled to

adsorption to the working electrode as a result of the decreased solubility of electrochemically generated oxidation products of Pd(dppf)TPT, giving rise to a second electrochemical oxidation event. We propose a mechanism wherein the initial Fc-centered oxidation is followed by an intermediate step in which the solubility of new oxidized species differs from the initial species, leading to adsorption onto the working electrode surface and the formation of films of partially-oxidized Pd(dppf)TPT. This modification of the working electrode is followed by a more complicated mechanism of electrochemical oxidation, which can likely be an implication of a fundamentally different electrode surface now being further oxidized at more positive potentials. Prolonged cycling of this oxidation chemistry results in depletion of all current, both oxidative and reductive, suggesting decomposition of the cage as evidenced by the lack of iron centers near the electrode. One possible explanation is that the remaining TPT building blocks fully passivate the electrode surface as it is non-redox-active within this potential window.

Overall, we have shown that the incorporation of multiple ferrocene centers into a discrete supramolecular cage directly influences the electrochemical reactivity of the species relative to free ferrocene. Understanding oxidation–reduction mechanisms and electron-transfer-induced changes of properties and reactivity of supramolecular assemblies is necessary to understand the electrochemical, chemical, and charge-transfer reactivity of such systems towards further developing their applications as multi-charge reservoirs for redox catalysis.

Supplementary Materials: The following supporting information can be downloaded at: <https://www.mdpi.com/article/10.3390/inorganics11030122/s1>, Spectroscopic characterization (UV-Vis, FT-ICR MS, NMR), electrochemical characterization by cyclic voltammetry, spectroelectrochemical UV-Vis measurements, and images of FTO Films (Figures S1–S22) (PDF), and Crystallographic data of Pd(dppf)TPT (CIF).

Author Contributions: A.B.G.: investigation, formal analysis, methodology, validation, visualization, writing. M.R.C.: investigation, formal analysis, writing—original draft. T.J.H.: investigation. Y.C.L.: formal analysis, methodology. D.F.W.: conceptualization, funding acquisition, methodology, project administration, resources, supervision, validation, writing—review and editing. T.R.C.: conceptualization, funding acquisition, methodology, project administration, resources, supervision, validation, writing—review and editing. All authors have read and agreed to the published version of the manuscript.

Funding: This work was supported by NSF CAREER Award #1847950 (TRC). This work utilized ICP-MS and a Fourier transform resonance mass spectrometer (FTMS) that was purchased with funding from an NSF Major Research Instrumentation Program (NSF CHE0959565).

Data Availability Statement: The data presented in this study are available in this article and the supplementary material provided.

Acknowledgments: The authors would like to thank Eric Jensen and the Chemistry Instrument Center and the Magnetic Resonance Center at the University at Buffalo. The authors would also like to thank Cornell University and Samantha MacMillan for crystallographic data acquisition.

Conflicts of Interest: The authors declare no conflict of interest.

References

1. Fabbrizzi, L. The ferrocenium/ferrocene couple: A versatile redox switch. *ChemTexts* **2020**, *6*, 22. [[CrossRef](#)]
2. Xu, L.; Wang, Y.-X.; Chen, L.-J.; Yang, H.-B. Construction of multiferrocenyl metallacycles and metallacages via coordination-driven self-assembly: From structure to functions. *Chem. Soc. Rev.* **2015**, *44*, 2148–2167. [[CrossRef](#)] [[PubMed](#)]
3. Young, D.J.; Chien, S.W.; Hor, T.S.A. 1,1'-Bis(diphenylphosphino)ferrocene in functional molecular materials. *Dalton Trans.* **2012**, *41*, 12655–12665. [[CrossRef](#)]
4. Musikhina, A.A.; Serebrennikova, P.O.; Zabelina, O.N.; Utepova, I.A.; Chupakhin, O.N. Advanced Application of Planar Chiral Heterocyclic Ferrocenes. *Inorganics* **2022**, *10*, 152. [[CrossRef](#)]
5. Tarafder, K.; Surendranath, Y.; Olshansky, J.H.; Alivisatos, A.P.; Wang, L.-W. Hole Transfer Dynamics from a CdSe/CdS Quantum Rod to a Tethered Ferrocene Derivative. *J. Am. Chem. Soc.* **2014**, *136*, 5121–5131. [[CrossRef](#)]

6. Paul, A.; Borrelli, R.; Bouyanfif, H.; Gottis, S.; Sauvage, F. Tunable Redox Potential, Optical Properties, and Enhanced Stability of Modified Ferrocene-Based Complexes. *ACS Omega* **2019**, *4*, 14780–14789. [[CrossRef](#)]
7. Erb, W.; Richy, N.; Hurvois, J.-P.; Low, P.J.; Mongin, F. From ferrocene to 1,2,3,4,5-pentafluoroferrrocene: Halogen effect on the properties of metallocene. *Dalton Trans.* **2021**, *50*, 16933–16938. [[CrossRef](#)]
8. Bennett, T.L.R.; Wilkinson, L.A.; Lok, J.M.A.; O'Toole, R.C.P.; Long, N.J. Synthesis, Electrochemistry, and Optical Properties of Highly Conjugated Alkynyl-Ferrocenes and -Biferrocenes. *Organometallics* **2021**, *40*, 1156–1162. [[CrossRef](#)]
9. Hsu, W.-C.; Wang, Y.-H. Homogeneous Water Oxidation Catalyzed by First-Row Transition Metal Complexes: Unveiling the Relationship between Turnover Frequency and Reaction Overpotential. *ChemSusChem* **2022**, *15*, e202102378. [[CrossRef](#)]
10. Singh, C.; Mukhopadhyay, S.; Hod, I. Metal–organic framework derived nanomaterials for electrocatalysis: Recent developments for CO₂ and N₂ reduction. *Nano Converg.* **2021**, *8*, 1. [[CrossRef](#)]
11. Mazzeo, A.; Santalla, S.; Gaviglio, C.; Doctorovich, F.; Pellegrino, J. Recent progress in homogeneous light-driven hydrogen evolution using first-row transition metal catalysts. *Inorg. Chim. Acta* **2021**, *517*, 119950. [[CrossRef](#)]
12. Kasprzak, A.; Nisiewicz, M.K.; Nowicka, A.M. A chromatography-free total synthesis of a ferrocene-containing dendrimer exhibiting the property of recognizing 9,10-diphenylanthracene. *Dalton Trans.* **2021**, *50*, 2483–2492. [[CrossRef](#)] [[PubMed](#)]
13. Brake, H.; Peresyphkina, E.; Virovets, A.V.; Kremer, W.; Klimas, C.; Schwarzmaier, C.; Scheer, M. Au-Containing Coordination Polymers Based on Polyphosphorus Ligand Complexes. *Inorg. Chem.* **2021**, *60*, 6027–6039. [[CrossRef](#)]
14. Kunde, T.; Pausch, T.; Guńka, P.A.; Krzyżanowski, M.; Kasprzak, A.; Schmidt, B.M. Fast, solvent-free synthesis of ferrocene-containing organic cages via dynamic covalent chemistry in the solid state. *Chem. Sci.* **2022**, *13*, 2877–2883. [[CrossRef](#)] [[PubMed](#)]
15. Kasprzak, A.; Kasprzak, N.; Kowalczyk, A.; Nowicka, A.M. Ferrocenylated 1,3,5-triphenylbenzenes for the electrochemical detection of various cations or anions. *Dalton Trans.* **2021**, *50*, 8426–8433. [[CrossRef](#)] [[PubMed](#)]
16. Vasdev, R.A.S.; Findlay, J.A.; Turner, D.R.; Crowley, J.D. Self-Assembly of a Redox Active, Metallosupramolecular [Pd₃L₆]⁶⁺ Complex Using a Rotationally Flexible Ferrocene Ligand. *Chem. Asian. J.* **2021**, *16*, 39–43. [[CrossRef](#)]
17. Kosińska, A.I.; Nisiewicz, M.K.; Nowicka, A.M.; Kasprzak, A. Electrochemical Recognition of Aromatic Species with Ferrocenylated 1,3,5-Triazine- or 1,3,5-Triphenylbenzene-Containing Highly Organized Molecules. *ChemPlusChem* **2021**, *86*, 820–826. [[CrossRef](#)]
18. Cook, T.R.; Zheng, Y.-R.; Stang, P.J. Metal-Organic Frameworks and Self-Assembled Supramolecular Coordination Complexes: Comparing and Contrasting the Design, Synthesis, and Functionality of Metal-Organic Materials. *Chem. Rev.* **2013**, *113*, 734–777. [[CrossRef](#)]
19. Cook, T.R.; Stang, P.J. Recent Developments in the Preparation and Chemistry of Metallacycles and Metallacages via Coordination. *Chem. Rev.* **2015**, *115*, 7001–7045. [[CrossRef](#)]
20. Pilloni, G.; Longato, B.; Corain, B. Heteropolymetallic complexes of 1,1'-bis(diphenylphosphino)ferrocene (dppf): VII. Redox behaviour of dppf. *J. Organomet. Chem.* **1991**, *420*, 57–65. [[CrossRef](#)]
21. Corain, B.; Longato, B.; Favero, G.; Ajò, D.; Pilloni, G.; Russo, U.; Kreissl, F.R. Heteropolymetallic complexes of 1,1'-Bis(diphenylphosphino)ferrocene (dppf). III. Comparative physicochemical properties of (dppf)MCl₂ (M = Co, Ni, Pd, Pt, Zn, Cd, Hg). *Inorganica Chim. Acta* **1989**, *157*, 259–266. [[CrossRef](#)]
22. Jiang, F.; Wang, J.; Li, J.; Wang, N.; Bao, X.; Wang, T.; Yang, Y.; Lan, Z.; Yang, R. Supramolecular Assemblies with Symmetrical Octahedral Structures—Synthesis, Characterization, and Electrochemical Properties. *Eur. J. Inorg. Chem.* **2013**, *2013*, 375–380. [[CrossRef](#)]
23. Chen, L.-J.; Li, Q.-J.; He, J.; Tan, H.; Abliz, Z.; Yang, H.-B. Design and Construction of Endo-Functionalized Multiferrocenyl Hexagons via Coordination-Driven Self-Assembly and Their Electrochemistry. *J. Org. Chem.* **2012**, *77*, 1148–1153. [[CrossRef](#)]
24. Ghosh, K.; Zhao, Y.; Yang, H.-B.; Northrop, B.H.; White, H.S.; Stang, P.J. Synthesis of a New Family of Hexakisferrocenyl Hexagons and Their Electrochemical Behavior. *J. Org. Chem.* **2008**, *73*, 8553–8557. [[CrossRef](#)]
25. Sun, S.-S.; Anspach, J.A.; Lees, A.J. Transition-metal directed self-assembly of adamantanoid-shaped supramolecules incorporating ferrocenyl moieties. *Inorganica Chim. Acta* **2003**, *351*, 363–368. [[CrossRef](#)]
26. Gray, H.B.; Sohn, Y.S.; Hendrickson, N. Electronic structure of metallocenes. *J. Am. Chem. Soc.* **1971**, *93*, 3603–3612. [[CrossRef](#)]
27. Ghosh, S.; Turner, D.R.; Batten, S.R.; Mukherjee, P.S. Self-assembly of a heterometallic molecular triangle using an ambidentate ligand and self-selection for a single linkage isomer. *Dalton Trans.* **2007**, *19*, 1869–1871. [[CrossRef](#)] [[PubMed](#)]
28. Stang, P.J.; Olenyuk, B.; Fan, J.; Arif, A.M. Combining Ferrocenes and Molecular Squares: Self-Assembly of Heterobimetallic Macrocyclic Squares Incorporating Mixed Transition Metal Systems and a Main Group Element. Single-Crystal X-ray Structure of [Pt(dppf)(H₂O)₂][OTf]₂. *Organometallics* **1996**, *15*, 904–908. [[CrossRef](#)]
29. Sun, S.-S.; Anspach, J.A.; Lees, A.J.; Zavalij, P.Y. Synthesis and Electrochemical, Photophysical, and Anion Binding Properties of Self-Assembly Heterometallic Cyclophanes. *Organometallics* **2002**, *21*, 685–693. [[CrossRef](#)]
30. Ferrer, M.; Mounir, M.; Rossell, O.; Ruiz, E.; Maestro, M.A. Equilibria between Metallosupramolecular Squares and Triangles with the New Rigid Linker 1,4-Bis(4-pyridyl)tetrafluorobenzene. Experimental and Theoretical Study of the Structural Dependence of NMR Data. *Inorg. Chem.* **2003**, *42*, 5890–5899. [[CrossRef](#)]
31. Haynes, W.M.; Lide, D.R.; Bruno, T.J. *CRC Handbook of Chemistry and Physics: A Ready-reference Book of Chemical and Physical Data*, 97th ed.; CRC Press: Boca Raton, FL, USA, 2016.
32. Macchioni, A.; Ciancaleoni, G.; Zuccaccia, C.; Zuccaccia, D. Determining accurate molecular sizes in solution through NMR diffusion spectroscopy. *Chem. Soc. Rev.* **2008**, *37*, 479–489. [[CrossRef](#)]

33. Chepelin, O.; Ujma, J.; Wu, X.; Slawin, A.M.Z.; Pitak, M.B.; Coles, S.J.; Michel, J.; Jones, A.C.; Barran, P.E.; Lusby, P.J. Luminescent, Enantiopure, Phenylatopyridine Iridium-Based Coordination Capsules. *J. Am. Chem. Soc.* **2012**, *134*, 19334–19337. [[CrossRef](#)]
34. Chakrabarty, R.; Mukherjee, P.S.; Stang, P.J. Supramolecular Coordination: Self-Assembly of Finite Two- and Three-Dimensional Ensembles. *Chem. Rev.* **2011**, *111*, 6810–6918. [[CrossRef](#)] [[PubMed](#)]
35. Komine, S.; Takahashi, S.; Kojima, T.; Sato, H.; Hiraoka, S. Self-Assembly Processes of Octahedron-Shaped Pd₆L₄ Cages. *J. Am. Chem. Soc.* **2019**, *141*, 3178–3186. [[CrossRef](#)] [[PubMed](#)]
36. Bard, A.J.; Faulkner, L.R. *Electrochemical Methods: Fundamentals and Applications*, 2nd ed.; Wiley: New York, NY, USA, 2001.
37. Ling, X.Y.; Reinhoudt, D.N.; Huskens, J. Ferrocenyl-Functionalized Silica Nanoparticles: Preparation, Characterization, and Molecular Recognition at Interfaces. *Langmuir* **2006**, *22*, 8777–8783. [[CrossRef](#)]
38. Kishore, P.V.V.N.; Liao, J.-H.; Hou, H.-N.; Lin, Y.-R.; Liu, C.W. Ferrocene-Functionalized Cu(I)/Ag(I) Dithiocarbamate Clusters. *Inorg. Chem.* **2016**, *55*, 3663–3673. [[CrossRef](#)] [[PubMed](#)]
39. MacDonald, D.G.; Kübel, C.; Corrigan, J.F. Ferrocenyl Functionalized Silver-Chalcogenide Nanoclusters. *Inorg. Chem.* **2011**, *50*, 3252–3261. [[CrossRef](#)]
40. Shayani-jam, H. Electrochemical study of adsorption and electrooxidation of 4,4'-biphenol on the glassy carbon electrode: Determination of the orientation of adsorbed molecules. *Monatsh. Chem.* **2019**, *150*, 183–192. [[CrossRef](#)]
41. Sohn, Y.S.; Hendrickson, D.N.; Gray, H.B. Electronic structure of ferricenium ion. *J. Am. Chem. Soc.* **1970**, *92*, 3233–3234. [[CrossRef](#)]
42. Weber, K.; Hockett, L.; Creager, S. Long-Range Electronic Coupling between Ferrocene and Gold in Alkanethiolate-based Monolayers on Electrodes. *J. Phys. Chem. B* **1997**, *101*, 8286–8291. [[CrossRef](#)]
43. Garah, M.E.; Cook, T.R.; Sepehrpour, H.; Ciesielski, A.; Stang, P.J.; Samori, P. Concentration-dependent supramolecular patterns of C3 and C2 symmetric molecules at the solid/liquid interface. *Colloids Surf. B* **2018**, *168*, 211–216. [[CrossRef](#)] [[PubMed](#)]
44. *CrysAlisPRO*; Oxford Diffraction/Agilent Technologies UK Ltd.: Yarnton, UK.
45. Sheldrick, G. SHELXT—Integrated space-group and crystal-structure determination. *Acta Crystallogr. Sect. A* **2015**, *71*, 3–8. [[CrossRef](#)] [[PubMed](#)]
46. Sheldrick, G. A short history of SHELX. *Acta Crystallogr. Sect. A* **2008**, *64*, 112–122. [[CrossRef](#)] [[PubMed](#)]

Disclaimer/Publisher's Note: The statements, opinions and data contained in all publications are solely those of the individual author(s) and contributor(s) and not of MDPI and/or the editor(s). MDPI and/or the editor(s) disclaim responsibility for any injury to people or property resulting from any ideas, methods, instructions or products referred to in the content.